Time-domain algorithm for single-photon laser-Doppler flowmetry at large interoptode spacing in human bone

Tiziano Binzoni,[1,2,*] Dimitri Van De Ville,[2,3] and Bruno Sanguinetti[4]

[1]Département de Neurosciences Fondamentales, University of Geneva, Switzerland

[2]Département de l'Imagerie et des Sciences de l'Information Médicale, University Hospital, Geneva, Switzerland

[3]Institute of Bioengineering, Ecole Polytechnique Fédérale de Lausanne (EPFL), Switzerland

[4]Group of Applied Physics, University of Geneva, Carouge, Switzerland

*Corresponding author: tiziano.binzoni@unige.ch

Received 22 July 2014; accepted 6 September 2014;
posted 10 September 2014 (Doc. ID 217350); published 15 October 2014

A new laser-Doppler flowmeter at large interoptode spacing, based on single-photon counting (single-photon laser-Doppler flowmetry [SP-LDF]) and allowing assessment of blood flow deep in bone tissue, is proposed and implemented. To exploit the advantages of the new SP-LDF hardware, a dedicated simple and efficient time-domain algorithm has been developed. The new algorithm is based on the zero-order moment of the power density spectrum of the *ad hoc* prefiltered photoelectric current. The SP-LDF has been validated by Monte Carlo simulations, as well as by experimental measurements on a bone tissue phantom for optical flowmeters and on human.

OCIS codes: (170.0170) Medical optics and biotechnology; (170.3660) Light propagation in tissues; (170.3340) Laser Doppler velocimetry.
http://dx.doi.org/10.1364/AO.53.007017

1. Introduction

Laser-Doppler flowmetry (LDF) at large interoptode spacing [1–6] allows the noninvasive assessment of deep tissue blood perfusion [7] in human bone [8], where the continuous and repeated assessment of blood perfusion has always been a difficult task [9,10]. It has been previously shown that LDF can monitor blood volume and blood perfusion kinetics in different human bones [11,12].

LDF at large interoptode spacing has in general a low signal-to-noise ratio (SNR); therefore, to observe, for example, blood flow pulsations, it is necessary to implement complex triggering procedures and use long acquisition times [12]. Low SNR may limit the depth of the monitored tissue regions of interest. The choice of the algorithm utilized to derive blood perfusion also has an influence on the maximum permitted LDF acquisition rate [13,14], limiting in some cases the potential of LDF.

Thus, to overcome some of these limitations we propose a new LDF working with a very sensitive detector, that is, a single-photon detector (SPD), based on a dedicated simple and fast algorithm. To distinguish the new LDF from the classical LDF, we name it single-photon LDF (SP-LDF).

2. Material and Methods

Section 2.A summarizes the classical algorithm for LDF. Section 2.B explains how to express the classical frequency-domain algorithm in the time domain. By taking into account the results of Section 2.B, in Section 2.C the new LDF algorithm is

1559-128X/14/307017-08$15.00/0

presented and an intuitive explanation is given in Section 2.E. In Section 2.F the mathematical link between the SP-LDF and laser-speckle contrast imaging (LSCI; see for a review [15]) is made. In Section 2.G, the SP-LDF hardware is described. The Monte Carlo (MC) and the experimental tests for the proposed SP-LDF are presented in Sections 2.H and 2.I, respectively.

A. Classical Algorithm for Laser-Doppler Flowmetry

A conventional LDF instrument at large interoptode spacing (d) is composed essentially of two parts: a continuous wave (CW) laser source and a detector generating the measured photoelectric current [$i(t)$, where t represents the time dependency]. The signal $i(t)$ is acquired during a finite time interval $t \in [-T, T]$. From $i(t)$ the number (m_i) of moving red blood cells (rbc) and the tissue blood perfusion (Φ_i) are classically assessed, in arbitrary units (a.u.), by [11]:

$$m_i = \frac{\langle \omega_i^0 \rangle}{\bar{\imath}^2}, \tag{1}$$

$$\Phi_i = \frac{\langle \omega_i^1 \rangle}{\bar{\imath}^2}, \tag{2}$$

where

$$\bar{\imath} = \frac{1}{2T} \int_{-T}^{+T} i(t) \mathrm{d}t, \tag{3}$$

and

$$\langle \omega_i^q \rangle := \int_{-\infty}^{+\infty} |\omega|^q \left| \int_{-\infty}^{+\infty} [i(t) - \bar{\imath}] \mathrm{e}^{-i\omega t} \mathrm{d}t \right|^2 \mathrm{d}\omega. \tag{4}$$

The roman i is the imaginary number and $q \in \{0, 1\}$. The term represented by the squared absolute value is the power density spectrum [$P_i(\omega)$] of $i(t)$ after subtracting the dc component; and thus Eq. (4) becomes:

$$\langle \omega_i^q \rangle = \int_{-\infty}^{+\infty} |\omega|^q P_i(\omega) \mathrm{d}\omega. \tag{5}$$

B. Classical Algorithm for Laser-Doppler Flowmetry Expressed in the Time Domain

Equation (5) can be equivalently expressed in the time domain as [14]:

$$\langle \omega_i^{2p} \rangle = \int_{-\infty}^{+\infty} \left| \frac{\mathrm{d}^p}{\mathrm{d}t^p} [i(t) - \bar{\imath}] \right|^2 \mathrm{d}t, \tag{6}$$

where the different moments, $\langle \omega_i^{2p} \rangle$, are written in terms of fractional derivatives [16] of order $p \in \{0, 1/2, 1, 3/2, \ldots\}$. From Eq. (6), Φ_i [Eq. (2)] can be derived by computing the fractional derivative of order 1/2. If implemented with optimized algorithms this might be a simpler solution than the use of the Fourier transform [Eq. (4)], but this is probably not the best. The zero-order moment, on the contrary, can be computed numerically in a very easy and efficient way by substituting $p = 0$ in Eq. (6). In fact, $\langle \omega_i^0 \rangle$ can be expressed as

$$\langle \omega_i^0 \rangle = \int_{-\infty}^{+\infty} (i(t) - \bar{\imath})^2 \mathrm{d}t, \tag{7}$$

which is easy to implement numerically. Unfortunately, Eq. (7) allows us to obtain m_i and not Φ_i [see Eq. (1)]. Thus, to take advantage of the efficient form of Eq. (7), in the present contribution we will express Φ_i in terms of $\langle \omega_i^0 \rangle$ (new algorithm) and *not* in terms of $\langle \omega_i^1 \rangle$ as it is classically done. The strategy allowing to reach this target consists in a suitable prefiltering of $i(t)$. The relevant point is that the prefiltering procedure will *not* increase the computation time because it is naturally generated by the SPD counter, part of the SP-LDF hardware. Thus, the new SP-LDF hardware and the new algorithm are strictly linked together, forming a unique instrumentation.

C. New Algorithm for Single-Photon-Laser-Doppler Flowmetry

The basis of the new time-domain algorithm can be summarized in four simple steps that will be further developed in the next subsections: (1) apply a finite impulse response (FIR) filter to $i(t)$ to obtain $i_\mathrm{f}(t)$; (2) apply a downsampling procedure to $i_\mathrm{f}(t)$ to obtain $i_{\mathrm{f}\downarrow}(n)$ (sampling time, Δt) where $n \in \mathbb{Z}$ is the time index; (3) compute the zero-order moment ($\langle \omega_{i_{\mathrm{f}\downarrow}}^0 \rangle$) of $i_{\mathrm{f}\downarrow}(n)$ by using a numerical implementation of Eq. (7); and (4) obtain the tissue blood perfusion ($\Phi_{i_{\mathrm{f}\downarrow}}$) by applying

$$\Phi_{i_{\mathrm{f}\downarrow}} := \left[\frac{\langle \omega_{i_{\mathrm{f}\downarrow}}^0 \rangle}{\bar{\imath}_{\mathrm{f}\downarrow}^2} \right]^{-1}, \tag{8}$$

where $\bar{\imath}_{\mathrm{f}\downarrow}$ is the mean value of $i_{\mathrm{f}\downarrow}(n)$.

It will be shown by MC simulations and experimental measurements on the bone phantom that

$$\Phi_{i_{\mathrm{f}\downarrow}} \propto \Phi_i, \tag{9}$$

that is, the new time-domain algorithm [Eq. (8)] gives the same (proportional) results as the classical method [Eq. (2)].

D. Filtering and Downsampling Applied to $i(t)$ to Generate $i_{\mathrm{f}\downarrow}(n)$

The FIR filter that is applied to $i(t)$, and allows obtaining $i_\mathrm{f}(t)$, is the moving average filter and can be expressed as

$$i_\mathrm{f}(t) = \frac{1}{\Delta t} \int_{-T}^{+T} i(t') \left[H\left(t' - t + \frac{\Delta t}{2}\right) - H\left(t' - t - \frac{\Delta t}{2}\right) \right] \mathrm{d}t'; \quad |t| \le T - \frac{\Delta t}{2}, \tag{10}$$

where H is the Heaviside function. The filter response, in the square brackets, is the rectangular function centered at t, with duration Δt, and unit amplitude.

The FIR filter represented by Eq. (10) is at the core of the new algorithm and the interesting point is that it is naturally "generated" by the use of the SPD counter. In fact, counting the photons detected by the SPD during the time intervals Δt is equivalent to Eq. (10). However, we must be aware that the SPD counter also introduces a downsampling operation because the samples are acquired only at specific instances $t = n\Delta t + \Delta t/2$ $(n \in \mathbb{Z})$, eventually generating $i_{f\downarrow}(n)$. Interestingly enough, due to the specific shape of the FIR filter, the downsampling has no influence on the measured parameters (see below). Figure 1 schematically illustrates the influence of the SPD counter on $i(t)$. The green circles represent the real $i_{f\downarrow}(n)$ signal acquired by the SP-LDF utilized in the experimental section, before any mathematical treatment.

To finish this section, we also note that experimentally the mean value of $i_f(t)$ can be expressed as

$$\bar{i}_f = \frac{1}{2\left(T - \frac{\Delta t}{2}\right)} \int_{-(T-\frac{\Delta t}{2})}^{+(T-\frac{\Delta t}{2})} i_f(t)\mathrm{d}t. \tag{11}$$

Combining Eqs. (10) and (11) leads to the observation that

$$\bar{i}_f \propto \bar{i}. \tag{12}$$

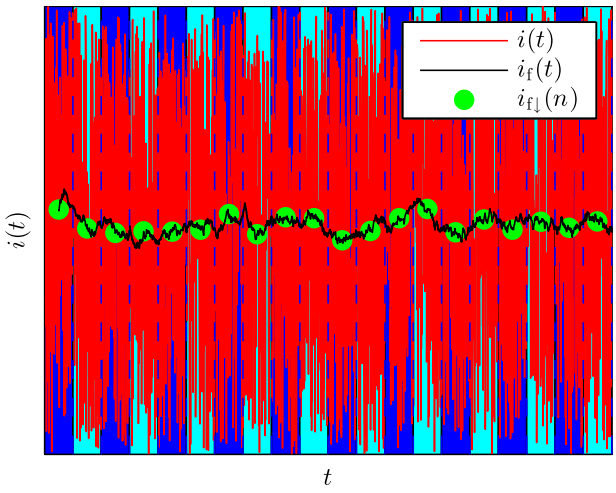

Fig. 1. Schematic drawing showing the LDF signal as a function of time (t) acquired by the SPD. $i(t)$ is the classical LDF photoelectric current as a function of t. $i_f(t)$ is $i(t)$ after filtering by a sliding window of width Δt. $i_{f\downarrow}(n)$ is the downsampled $i_f(t)$ at a sampling time of Δt. $i_{f\downarrow}(n)$ is the actual signal recorded by the SP-LDF on which Eq. (8) will be applied. The parameter $n \in \mathbb{Z}$ represents the time sampled at discrete values. The vertical blue/cyan bars represent the Δt time intervals.

E. Intuitive Explanation of the New Single-Photon-Laser-Doppler Flowmetry Algorithm

To have better insight into how the Eq. (8) algorithm works, we must compare the power density spectra of $i(t)$ and $i_f(t)$ $[P_{i_f}(\omega)]$. If the FIR filter [Eq. (10)] is applied to $i(t)$ it is straightforward to show that

$$P_{i_f}(\omega) = \left|\mathrm{sinc}\left(\frac{\Delta t\omega}{2\pi}\right)\right|^2 P_i(\omega), \tag{13}$$

where $\mathrm{sinc}(x) := \sin(\pi x)/(\pi x)$. From classical LDF, we know that $\langle\omega_i^0\rangle$ is insensitive to tissue blood speed changes because an increase in speed increases the frequency range spanned by $P_i(\omega)$ but maintains the same area under the curve [Figs. 2(a) and 2(b), red and cyan surfaces are the same]. However, if we apply the FIR filter [black curve in Figs. 2(a) and 2(b)], we obtain $P_{i_f}(\omega)$ represented in Figs. 2(c) and 2(d), and in this case an increase in blood speed induces a decrease in the $P_{i_f}(\omega)$ surface; that is, a decrease in $\langle\omega_{i_f}^0\rangle$. Thus, the zero-order moment becomes sensitive also to the blood speed.

The illustration of Fig. 2 provides us with an intuitive explanation why $\langle\omega_{i_f}^0\rangle$ becomes sensitive also to blood speed and thus to blood perfusion, but, in practice, we will use $\langle\omega_{i_{f\downarrow}}^0\rangle$ and not $\langle\omega_{i_f}^0\rangle$. Thus, it is necessary to clarify precisely the exact link between $\langle\omega_{i_f}^0\rangle$ and $\langle\omega_{i_{f\downarrow}}^0\rangle$. Figure 3 shows the influence of the $i_f(t)$ undersampling on $P_{i_f}(\omega)$. It is well known that the undersampling folds the spectrum $P_{i_f}(\omega)$ [Fig. 3(a)] at $\pm\nu_o$, the Nyquist frequency, and all integer (k) multiples of ν_o. This restricts the spectrum essentially to the interval $[-\nu_o, \nu_o]$. Figure 3(b) shows how $P_{i_f}(\omega)$ is folded; the sum of all the curves finally

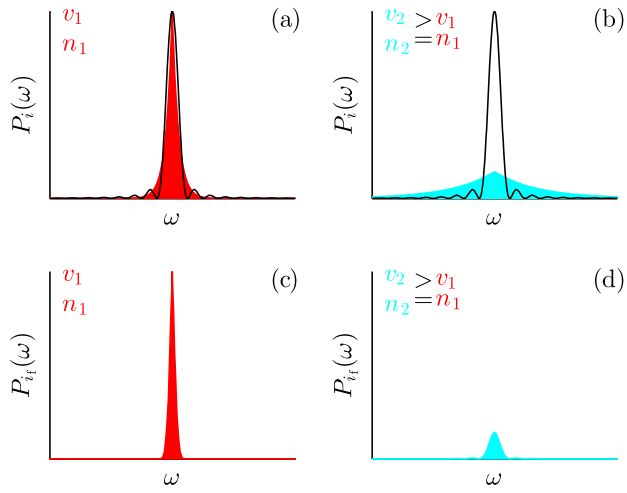

Fig. 2. (a) Classical LDF spectrum $[P_i(\omega)$, red] for a mean rbc speed, v_1, and number of rbc, n_1; (b) classical LDF spectrum $[P_i(\omega)$, cyan] for a mean rbc speed, v_2, and number of rbc, n_2; (c) LDF spectrum $[P_{i_f}(\omega)]$ obtained after filtering $P_i(\omega)$ in panel (a) with the filter appearing in black in panel (a); (d) LDF spectrum $[P_{i_f}(\omega)]$ obtained after filtering $P_i(\omega)$ in panel (b) with the filter appearing in black in panel (b). (c) and (d) are obtained from (a) and (b), respectively, by applying Eq. (13).

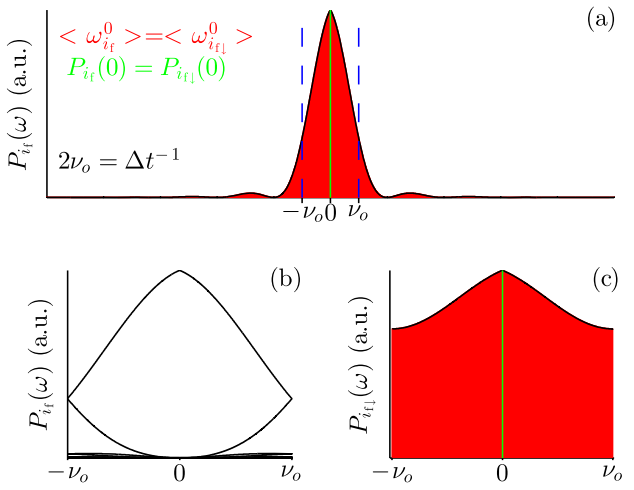

Fig. 3. (a) Schematic drawing showing the resulting LDF power density spectrum $[P_{i_f}(\omega)]$ if the spectrum is filtered by an FIR filter [Eq. (13)] with parameter Δt. Vertical dashed bars determine the region where the spectrum is folded if we apply an undersampling of sampling time Δt to i_f. The red region represents $\langle \omega^0_{i_f} \rangle$, that is, the $P_{i_f}(\omega)$ surface. (b) Illustration of how $P_{i_f}(\omega)$ is folded inside the interval $[-\nu_o, \nu_o]$; (c) resulting spectrum after undersampling $[P_{i_{f\downarrow}}(\omega)]$. $P_{i_{f\downarrow}}(\omega)$ is the sum of all the curves in panel (b). The red surface in panel (a) is equal to that in panel (c), that is, $\langle \omega^0_{i_f} \rangle = \langle \omega^0_{i_{f\downarrow}} \rangle$. The vertical green lines in panel (a) and (c) show that $P_{i_f}(0) = P_{i_{f\downarrow}}(0)$.

gives $P_{i_{f\downarrow}}(\omega)$ [Fig. 3(c)]. The important conclusion here is that the red areas in Figs. 3(a) and 3(c) have the same surface and thus

$$\langle \omega^0_{i_f} \rangle = \langle \omega^0_{i_{f\downarrow}} \rangle. \tag{14}$$

Moreover, one can also see that

$$P_{i_f}(0) = P_{i_{f\downarrow}}(0), \tag{15}$$

because the filter is zero for all multiples $2k\nu_o$ and these points always fall at the origin after folding [Fig. 3(b)]. Considering that the value of the power density spectrum at the origin is mathematically equal to the mean of the data in the time domain, this implies that

$$\bar{i}_f = \bar{i}_{f\downarrow}, \tag{16}$$

and thus from Eqs. (8), (14), and (16),

$$\Phi_{i_f} = \Phi_{i_{f\downarrow}}. \tag{17}$$

All conclusions derived in the present context for Φ_{i_f} remain valid also for $\Phi_{i_{f\downarrow}}$.

We can now further investigate the relationship between $\langle \omega^0_{i_{f\downarrow}} \rangle$ (or its normalized form by $\bar{i}^2_{f\downarrow}$) and the combined influence of the rbc number and the blood flow velocity, that is, blood perfusion. This will be studied in the following sections through MC simulations and measurements on bone phantom.

F. Link between Single-Photon-Laser-Doppler Flowmetry and Laser-Speckle Contrast Imaging

For the implementation of Eq. (8) on a real SP-LDF system, one applies the discrete version of Eq. (7), and Eq. (8) can be expressed as

$$\Phi_{i_{f\downarrow}} \propto \frac{\bar{i}^2_{f\downarrow}}{\sum_{n=1}^{N} (i_{f\downarrow}(n) - \bar{i}_{f\downarrow})^2}, \tag{18}$$

where

$$\bar{i}_{f\downarrow} = \frac{1}{N} \sum_{n=1}^{N} i_{f\downarrow}(n). \tag{19}$$

To reveal the link between SP-LDF and LSCI, we multiply Eq. (18) by the constant term, N:

$$\Phi_{i_{f\downarrow}} \propto \left[\frac{1}{\bar{i}^2_{f\downarrow}} \frac{\sum_{n=1}^{N} (i_{f\downarrow}(n) - \bar{i}_{f\downarrow})^2}{N} \right]^{-1}. \tag{20}$$

This operation will not change the information we need because $\Phi_{i_{f\downarrow}}$ is in any case expressed in a.u. From Eq. (20), we identify the variance (σ^2) of $i_{f\downarrow}(n)$ and thus:

$$\Phi_{i_{f\downarrow}} \propto \left[\frac{\sigma^2}{\bar{i}^2_{f\downarrow}} \right]^{-1} := C^{-2}. \tag{21}$$

Equation (21) clearly reproduces the algorithm utilized in temporal LSCI, where C is termed the "contrast" and C^{-2} is proportional to the blood flow, $\Phi_{i_{f\downarrow}}$ [17] (see Section 4.C for a discussion).

G. Single-Photon-Laser-Doppler Flowmetry Hardware

The SP-LDF (see Fig. 4) consisted of a 785 nm CW laser source (IRLD50, Moor Instruments Ltd.) and a nonparalyzable SPD (PCDMini-s0020, SensL) with an ~1% quantum efficiency at 785 nm, dead time 100 ns and sensor active area 20 μm. A counter (NI USB-6251, National Instruments Corporation) with a maximum count rate of 20 MHz was connected to the transistor-transistor logic (TTL) output of the SPD. The photons were counted during N consecutive time intervals of duration $\Delta t = 5$ ms each, obtaining N measurements of $i_{f\downarrow}(n)$. A 1.5 m (Moor Instruments Ltd.) multimode optical fiber (core diameter 400 μm) was connected to the laser. Another 2 m (Huber + Suhner) single-mode optical fiber (core diameter 62.5 μm) was connected to the SPD. The acquisition software and data treatment was written in the MATLAB language (Mathworks Inc.).

H. Monte Carlo Simulations

Following the procedure previously presented by Binzoni *et al.* [11], parallel MC simulations were performed on a 12-nodes PC cluster (12× Pentium 4, 3 GHz), for an interoptode distance of $d = 30$ mm. The rbc velocity was modeled for a normal distribution of the velocity components (root mean square

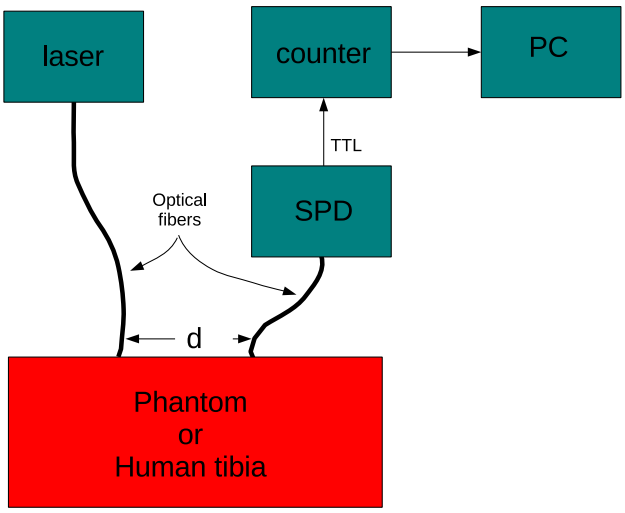

Fig. 4. Schematic drawing representing the new laser-Doppler flowmeter (SP-LDF). SPD, single-photon detector.

velocity, $\langle V^2_{\text{Brown}}\rangle^{1/2}$) [18,19]. The optical and physiological parameters for the bone tissue were chosen as all the combinations of the following values [11,20,21]: $\langle V^2_{\text{Brown}}\rangle^{1/2} \in \{0.5, 1, 1.5, 2, 1.5, 3\}$ mm s^{-1}, $\mu'_s \in \{0.9, 1, 1.1\}$ mm^{-1} (reduced scattering coefficient), $\mu_a \in \{0.004, 0.005, 0.006\}$ mm^{-1} (absorption coefficient), $n = 1.4$ (refractive index), $g \in \{0.5, 0.9\}$ (anisotropy parameter), and $P_{\text{move}} \in \{0.006, 0.008, 0.01, 0.045, 0.05, 0.055\}$ (probability that a photon interacts with a moving scatterer, i.e., rbc). In the MC simulations, each combination of these parameters leads to a spectrum $P_i(\omega)$ and, by applying Eq. (13) with $\Delta t = 5$ ms, to $P_{i_f}(\omega)$. Then, from $P_i(\omega)$ and $P_{i_f}(\omega)$, the parameters $\langle\omega_i^1\rangle$, $\bar{\imath}$, $\langle\omega_{i_f}^0\rangle$, and $\bar{\imath}_f$ [proportional to $\bar{\imath}$; see Eq. (12)] were computed. With these parameters the well-known classical LDF and the new SP-LDF were compared, that is, the validity of Eq. (9) was tested.

I. Experimental Measurements

1. *Measurements on Flow Phantom*

A bone tissue phantom for optical flowmeters, allowing vascular-to-whole tissue volume fractions of 0.19, 0.1267, and 0.0634, has been used to test the SP-LDF [22]. The flow, Φ, was controlled by a peristaltic pump (minipuls 2, Gilson) resulting in a range of $\Phi \in [0, 2]$ ml min^{-1}. The minimal non-nil value $\Phi \approx 0.1$ ml min^{-1} was determined by the characteristics of the experimental setup. Lower values can be detected. Standardized homogenized fresh cow milk (3.9% fat) was used as a circulating fluid. Milk was diluted in bidistilled water (2 ml of milk for a total of 500 ml of water-milk mixture).

2. *Test on Human Tibia*

The subject was comfortably seated on a chair with the feet lying on an elevated (10 cm) support. The optodes were placed on the right tibial diaphysis (medial surface) at the half-distance between the medial malleolus and the medial condyle, along the main axis of the tibia. A dedicated pneumatic tourniquet for legs (Riester komprimeter, Rudolf Riester GmbH) was placed around the right thigh. An average of two acquisitions with $d = 30$ mm, $N = 128$ (same N appearing in section 2.F), $\Delta t = 5$ ms each was used to obtain a $\Phi_{i_{f\downarrow}}$ value. The flow $\Phi_{i_{f\downarrow}}$ was assessed in real time, with a time resolution of ~1.67 s ($2 * N\Delta t = 1.28$ s plus data transfer, computing, and display time), during 1 min baseline, 2 min arterial occlusion (tourniquet inflated at 400 mmHg), and 2 min reperfusion (tourniquet at ambient pressure).

3. Results

A. Monte Carlo Simulations

Figure 5 shows the MC simulations comparing the classical LDF to the new SP-LDF. The total computation time was ~9 days. One can see that SP-LDF perfectly reproduces the behavior of a classical LDF at large interoptode spacing (coefficient of determination $R^2 \approx 1$). The small deviations from the linear relationship are due to the normal MC "noise." This result confirms the validity of Eq. (9) and the possibility to use $\Phi_{i_{f\downarrow}}$ to assess tissue blood perfusion as it is usually done with classical LDF at large interoptode spacing.

B. Experimental Measurements

1. *Measurements on Bone Flow Phantom*

Figure 6 shows $\Phi_{i_{f\downarrow}}$ as a function of the actual flow Φ on the bone tissue phantom. The high coefficient of determination $R^2 = 0.95$ further confirms the reasonable validity of the SP-LDF method in real settings and its sensitivity to flow changes.

2. *Test on Human Tibia*

Figure 7 shows $\Phi_{i_{f\downarrow}}$ as a function of time, during the baseline-ischemia-reperfusion protocol performed on

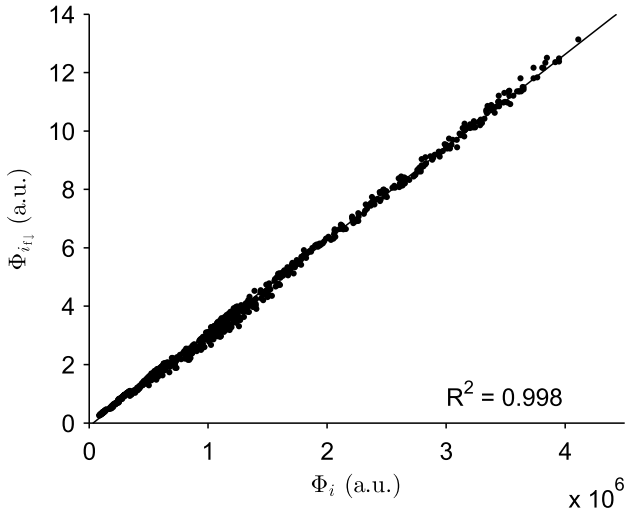

Fig. 5. MC simulations, for $d = 30$ mm, comparing tissue blood perfusion measurements, Φ_i, assessed by the classical LDF, and the new SP-LDF method, $\Phi_{i_f} = \Phi_{i_{f\downarrow}}$ [Eq. (17)].

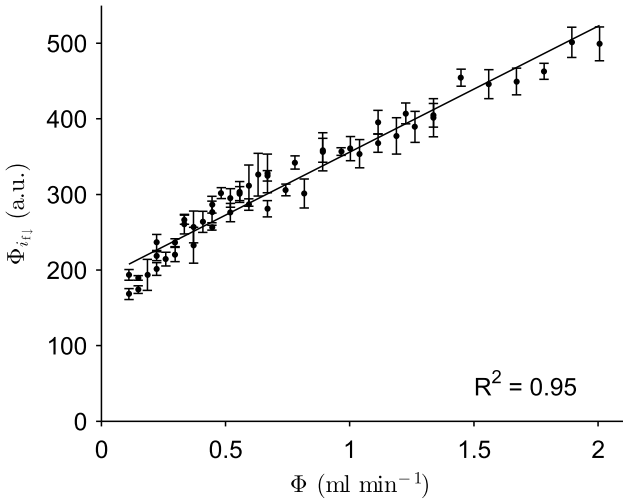

Fig. 6. Perfusion, $\Phi_{i_{f\downarrow}}$, measured by SP-LDF on the bone phantom as a function of the actual milk flow, Φ. $\Delta t = 5$ ms, $N = 128$, and $d = 30$ mm. Vertical bars indicate standard deviations (five measurements).

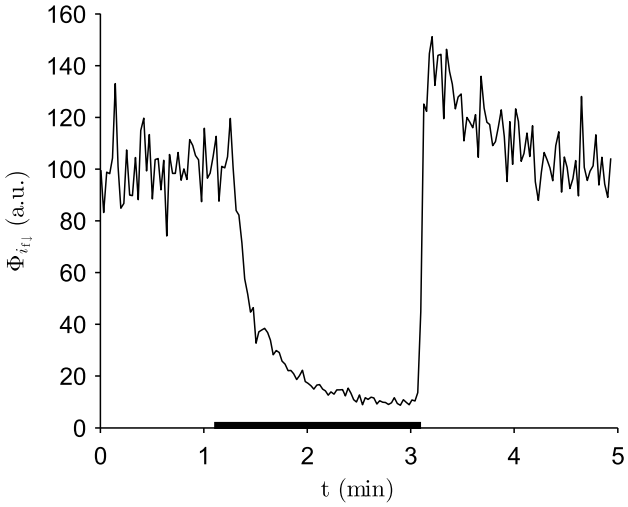

Fig. 7. Human tibia diaphysis blood flow, $\Phi_{i_{f\downarrow}}$, as a function of time, t, for $d = 30$ mm. The thick black line corresponds to the arterial occlusion time period. $\Delta t = 5$ ms and $N = 128$.

the human tibia diaphysis. As expected, the hyperemic postischemic response is clearly visible as an increase above the baseline after 3 min.

4. Discussion and Conclusions

In the present contribution we have shown that it is possible to assess tissue blood perfusion, $\Phi_{i_{f\downarrow}}$, in humans by means of SP-LDF at large interoptode spacing by single-photon counting. To this aim, an efficient new time-domain algorithm [Eq. (8)], based on the estimation of a zero-order moment in the time domain [Eq. (18)], has been applied.

A. Monte Carlo Simulations

MC simulations utilized in the present contribution have already been used in the past for different source detector separations [11]. The MC simulations take into account the multiple scattering regime observed at large interoptode spacing [23], and thus they are ideal for the present context. The validity of the MC simulations compared to real data was also previously studied, for example, by Kienle *et al.* [24]. Thanks to this approach, in the present work, we have shown that the Eq. (18) algorithm for SP-LDF allows obtaining the same flow values, in a.u., as classical LDF. This means that SP-LDF has the same linear dependence on tissue perfusion as LDF but with the advantage of the very high sensitivity given by the SPD. In fact, a classical LDF, using, for example, a single avalanche photo detector, is not able to acquire data at a sampling rate of 1.67 s (Section 2.I.2) and $d = 30$ mm.

B. Experimental Measurements

1. *Measurements on Bone Flow Phantom*

As expected from MC simulations, measurements on bone flow phantom also show that $\Phi_{i_{f\downarrow}}$ is linearly related to real flow changes. The flow has been determined over a range of values reasonably expected in *in vivo* bone. Measurements have been performed on a homogeneous flow phantom where the flow distribution is uniform over all the phantom. It remains to study the behavior of SP-LDF in the case of more complex flow distributions, but this necessitates more complex phantoms. This topic certainly deserves future investigations.

2. *Test on Human Tibia*

Figure 7 reports $\Phi_{i_{f\downarrow}}$ assessed on human tibia diaphysis during baseline, ischemia, and reperfusion periods. The expected postischemic hyperemic peak appears after 3 min immediately after the cuff release. As expected, during ischemia $\Phi_{i_{f\downarrow}}$ goes to a minimum value but not to zero. This behavior is also observed in classical LDF and is called in the literature "biological zero" [25,26]. For the current measurements this baseline level includes the remaining Brownian movement generated by the moving scatterers (e.g., lipid droplets acting similar to rbc) contained in the fluid. *In vivo* the "biological zero" may also account for other phenomena, such as residual vessels' movement.

As noted in Section 4.A, SP-LDF has a greater sensitivity if compared to classical LDF. However, it must also be pointed out that the quantum efficiency of the SPD utilized for the proposed measurements was actually low (~1%). More recent SPDs may have a quantum efficiency >40% at 785 nm. Thus, one can expect to be able to work even at larger d with a better and commercially available detector. Moreover, the simultaneous use of multiple SPDs in parallel will certainly contribute to a further improvement of the system. The use of the proposed new algorithm may also represent an efficient solution to treat the signal coming from a large number of detectors simultaneously.

C. Link between Single-Photon-Laser-Doppler Flowmetry and Laser-Speckle Contrast Imaging

Although SP-LDF and LSCI share the same algorithm (Section 2.F), they come with different optical setups. In fact, SP-LDF uses a point source, while LSCI uses a large spot of light. At first sight, this may seem incompatible; however, another well-known example has this particularity. This is the case for full-field laser-Doppler imaging (FFLDI [27–29]), where LDF and FFLDI use the same algorithm but have different light source configurations (i.e., FFLDI has the same source configuration as LSCI). Moreover, we must also not forget that LSCI is strongly linked to LDF [30–32] because basically they are describing the same physical phenomenon. Thus, the strong link between SP-LDF and LSCI does not come as a surprise in the end.

Considering the link existing between SP-LDF and LSCI, in the present contribution a typical Δt value utilized in LSCI has been used. However, as is the case for LSCI, other Δt values can be considered, but future methodical studies on this topic will be necessary if one wants to find the optimal Δt range of values.

The interesting point that ensues from the SP-LDF/LSCI relationship is that there exists a well-known "spatial" version of Eq. (21) for LSCI [15]. In practice σ and $\bar{i}_{f\downarrow}$ are obtained by considering a group of pixels in a small region of interest. In analogy with this approach, it would be extremely interesting to use a bundle of detection fibers in SP-LDF (with the relative SPDs) and translate Eq. (21) in the spatial domain also for SP-LDF. If it works, as can be theoretically expected, this should drastically reduce the $\Phi_{i_{f\downarrow}}$ sampling time for the SP-LDF instrumentation. Future studies should investigate how this can open a new approach for blood flow monitoring deep in human bone.

D. Conclusions

It has been demonstrated that SP-LDF is an effective optical technique allowing the noninvasive monitoring of bone blood flow. SP-LDF technique is promising to open new ways for the study of bone blood flow regulation mechanisms in humans.

The authors kindly thank Professor Hugo Zbinden (GAP, University of Geneva) for lending them the SPD.

References and Notes

1. R. Bonner and R. Nossal, "Model for laser Doppler measurements of blood flow in tissue," Appl. Opt. **20**, 2097–2107 (1981).
2. G. Soelkner, G. Mitic, and R. Lohwasser, "Monte Carlo simulations and laser Doppler flow measurements with high penetration depth in biological tissuelike head phantoms," Appl. Opt. **36**, 5647–5654 (1997).
3. R. Lohwasser and G. Soelkner, "Experimental and theoretical laser-Doppler frequency spectra of a tissuelike model of a human head with capillaries," Appl. Opt. **38**, 2128–2137 (1999).
4. R. G. M. Kolkman, E. Hondebrink, R. A. Bolt, W. Steenbergen, and F. F. M. de Mul, "Pulsed laser-doppler flowmetry for monitoring deep perfusion," Proc. SPIE **4434**, 204–207 (2001).
5. T. Binzoni, T. S. Leung, D. Boggett, and D. Delpy, "Non-invasive laser Doppler perfusion measurements of large tissue volumes and human skeletal muscle blood RMS velocity," Phys. Med. Biol. **48**, 2527–2549 (2003).
6. A. Humeau, W. Steenbergen, H. Nilsson, and T. Stromberg, "Laser Doppler perfusion monitoring and imaging: novel approaches," Med. Biol. Eng. Comput. **45**, 421–435 (2007).
7. We will consider in this contribution only LDFs at large interoptode spacing, i.e., LDFs whose source/detector separation is, e.g., ≥1.5 cm. LDF does not produce perfusion images but gives the mean blood perfusion of a tissue "volume."
8. T. Binzoni and D. Van De Ville, "Noninvasive probing of the neurovascular system in human bone/bone marrow using near-infrared light," J. Innov. Opt. Health Sci. **4**, 183–189 (2011).
9. M. Brookes and W. Revell, *Blood Supply of Bone: Scientific Aspects* (Springer, 1998).
10. J. P. Dyke and R. K. Aaron, "Noninvasive methods of measuring bone blood perfusion," Ann. N.Y. Acad. Sci. **1192**, 95–102 (2010).
11. T. Binzoni, D. Boggett, and D. Van De Ville, "Laser-Doppler flowmetry at large interoptode spacing in human tibia diaphysis: Monte Carlo simulations and preliminary experimental results," Physiol. Meas. **32**, N33–N53 (2011).
12. T. Binzoni, D. Tchernin, J. N. Hyacinthe, D. Van De Ville, and J. Richiardi, "Pulsatile blood flow in human bone assessed by laser-Doppler flowmetry and the interpretation of photoplethysmographic signals," Physiol. Meas. **34**, N25–N40 (2013).
13. M. Draijer, E. Hondebrink, T. van Leeuwen, and W. Steenbergen, "Time domain algorithm for accelerated determination of the first order moment of photo current fluctuations in high speed laser Doppler perfusion imaging," Med. Biol. Eng. Computing **47**, 1103–1109 (2009).
14. T. Binzoni, C. S. Seelamantula, and D. Van De Ville, "A fast time-domain algorithm for the assessment of tissue blood flow in laser-Doppler flowmetry," Phys. Med. Biol. **55**, N383–N394 (2010).
15. D. A. Boas and A. K. Dunn, "Laser speckle contrast imaging in biomedical optics," J. Biomed. Opt. **15**, 011109 (2010).
16. I. Podlubny, *Fractional Differential Equations: An Introduction to Fractional Derivatives, Fractional Differential Equations, Some Methods of Their Solution and Some of Their Applications* (Academic, 1999).
17. H. Cheng, Y. Yan, and T. Q. Duong, "Temporal statistical analysis of laser speckle images and its application to retinal blood-flow imaging," Opt. Express **16**, 10214–10219 (2008).
18. J. Zhong, A. M. Seifalian, G. E. Salerud, and G. E. Nilsson, "A mathematical analysis on the biological zero problem in laser Doppler flowmetry," IEEE Trans. Biomed. Eng. **45**, 354–364 (1998).
19. T. Binzoni, T. S. Leung, M. L. Seghier, and D. T. Delpy, "Translational and Brownian motion in laser-Doppler flowmetry of large tissue volumes," Phys. Med. Biol. **49**, 5445–5458 (2004).
20. P. Farzam, P. Zirak, T. Binzoni, and T. Durduran, "Pulsatile and steady-state hemodynamics of the human patella bone by diffuse optical spectroscopy," Physiol. Meas. **34**, 839–857 (2013).
21. A. Kienle, "Non-invasive determination of muscle blood flow in the extremities from laser Doppler spectra," Phys. Med. Biol. **46**, 1231–1244 (2001).
22. T. Binzoni, A. Torricelli, R. Giust, B. Sanguinetti, P. Bernhard, and L. Spinelli, "Bone tissue phantoms for optical flowmeters at large interoptode spacing generated by 3D-stereolithography," Biomed. Opt. Express **5**, 2715–2725 (2014).
23. F. F. de Mul, M. H. Koelink, M. L. Kok, P. J. Harmsma, J. Greve, R. Graaff, and J. G. Aarnoudse, "Laser Doppler velocimetry and Monte Carlo simulations on models for blood perfusion in tissue," Appl. Opt. **34**, 6595–6611 (1995).
24. A. Kienle, M. S. Patterson, L. Ott, and R. Steiner, "Determination of the scattering coefficient and the anisotropy factor from laser Doppler spectra of liquids including blood," Appl. Opt. **35**, 3404–3412 (1996).
25. T. Tenland, E. G. Salerud, G. E. Nilsson, and P. A. Oberg, "Spatial and temporal variations in human skin blood flow," Int. J. Microcirc. Clin. Exp. **2**, 81–90 (1983).

26. D. P. Kernick, J. E. Tooke, and A. C. Shore, "The biological zero signal in laser Doppler fluximetry—origins and practical implications," Pflügers Arch. **437**, 624–631 (1999).
27. A. Serov, W. Steenbergen, and F. de Mul, "Laser Doppler perfusion imaging with a complimentary metal oxide semiconductor image sensor," Opt. Lett **27**, 300–302 (2002).
28. A. Serov, B. Steinacher, and T. Lasser, "Full-field laser Doppler perfusion imaging and monitoring with an intelligent CMOS camera," Opt. Express **13**, 3681–3689 (2005).
29. A. Serov and T. Lasser, "High-speed laser Doppler perfusion imaging using an integrating CMOS image sensor," Opt. Express **13**, 6416–6428 (2005).
30. J. D. Briers, "Laser doppler and time-varying speckle: a reconciliation," J. Opt. Soc. Am. A **13**, 345–350 (1996).
31. M. J. Draijer, E. Hondebrink, M. Larsson, T. G. van Leeuwen, and W. Steenbergen, "Relation between the contrast in time integrated dynamic speckle patterns an the power spectral density of their temporal intensity fluctuations," Opt. Express **18**, 21883–21891 (2010).
32. O. B. Thompson and M. K. Andrews, "Tissue perfusion measurements: multiple-exposure laser speckle analysis generates laser Doppler-like spectra," J. Biomed. Opt. **15**, 027015 (2010).